# 3D Ordered Mesoporous Bifunctional Oxygen Catalyst for Electrically Rechargeable Zinc–Air Batteries

*Moon Gyu Park, Dong Un Lee, Min Ho Seo, Zachary Paul Cano, and Zhongwei Chen**

With increasing costs of natural fuels and environmental issues associated with their use, novel battery technologies such as metal–air batteries are attracting much attention due to their extremely high energy density compared to currently most widely used lithium–ion batteries.[1–3] Since metal–air batteries utilize oxygen in atmospheric air as cathodic fuel, no on-board fuel reservoir is required, making them highly viable for electric vehicle applications. Currently, however, a few technical challenges hamper widespread commercialization of metal–air batteries such as slow kinetics of oxygen reduction reaction (ORR) and oxygen evolution reaction (OER), which are the electrochemical reactions that govern discharge and charge processes of the battery. Relatively large overpotentials associated with these reactions leads to poor energy efficiencies, which motivates research and development of active catalysts that can enhance the reaction kinetics.

Currently, metal–air battery investigations are much focused on the development of bifunctionally active and durable catalysts to enhance both ORR and OER using inexpensive, Earth-abundant, and environmentally friendly materials. As a family of nonprecious electrocatalysts, transition metal-based catalysts have been rigorously investigated and utilized as the bifunctional catalysts for metal–air batteries.[4–14] In particular, transition metal oxides have attracted much attention for bifunctional application due to their exceptional activity and stability since they possess multiple valences and abundant crystallographic structures resulting in rich redox electrochemistry and materials chemistry, providing a vast opportunity.[15–21] However, more rigorous research effort is required to further improve the catalytic activity and stability potentially by altering chemical compositions, morphologies, or crystal structures. Among various nonprecious metal oxide catalysts, spinel cobalt oxides ($Co_3O_4$) having different morphologies, such as nanoparticles, nanowires, and nanoflakes, are widely utilized as efficient bifunctional electrocatalysts, demonstrating enhanced catalytic activity and electrochemical stability.[8,22–25] Among previous research of spinel cobalt oxides as bifunctional catalysts in our group, $Co_3O_4$ nanodisks and nanowires have been prepared with enhanced active surface area accompanied by improved ORR and OER activities.[26,27] Especially, $Co_3O_4$ nanowires directly grown on stainless steel mesh have provided a promising possibility of a practically usable rechargeable zinc–air battery by demonstrating a long durability. However, their performance until now is still insufficient to be commercially mass produced for widespread usage. To further advance the performance of nonprecious metal catalysts, it is necessary to develop 3D structures, possessing highly porous and stable architectures that can generate excellent catalytic activity and stability.

Herein, we introduce hierarchically porous and structurally robust 3D ordered mesoporous cobalt oxide (3DOM $Co_3O_4$), a nonprecious bifunctional catalyst active towards both ORR and OER as a promising air electrode material for electrically rechargeable zinc–air batteries. This innovative electrocatalyst with advanced morphology is synthesized by a simple template-derived process. Polystyrene (PS) bead templates are prepared and soaked in cobalt precursor solution where the precursor permeates the voids of the beads followed by heat treatment and dissolution process to crystallize cobalt oxide frames and remove polystyrenes, respectively. 3DOM $Co_3O_4$ is a highly promising candidate for nonprecious bifunctional catalysts due to its significantly extended active surface area and highly stable structure which are derived from 3D and hierarchically ordered pores and considerably robust metal oxide architecture, respectively. Utilizing the advanced electrocatalyst, highly bifunctional activity and durability are demonstrated by three electrode half-cell testing and electrically rechargeable zinc–air battery cycling as fundamental and practical electrochemical evaluation techniques, respectively.

**Figure 1** shows a simple schematic process of 3DOM $Co_3O_4$ synthesis, transmission electron microscopy (TEM) images, and a high-resolution TEM (HRTEM) image with

M. G. Park, D. U. Lee, Dr. M. H. Seo, Z. P. Cano, Prof. Z. Chen
Department of Chemical Engineering
Applied Nanomaterials and Clean Energy Laboratory
University of Waterloo
Waterloo ON N2L 3G1, Canada
E-mail: zhwchen@uwaterloo.ca

Dr. M. H. Seo
Hydrogen & Fuel Cell Center for Industry, Academy, and Laboratories
New & Renewable Energy Research Division
Korea Institute of Energy Research (KIER)
Sinjaesaengeneogi-ro, Haseo-myeon, Buan-gun, Jellabuk-do 56332
South Korea

DOI: 10.1002/smll.201600051

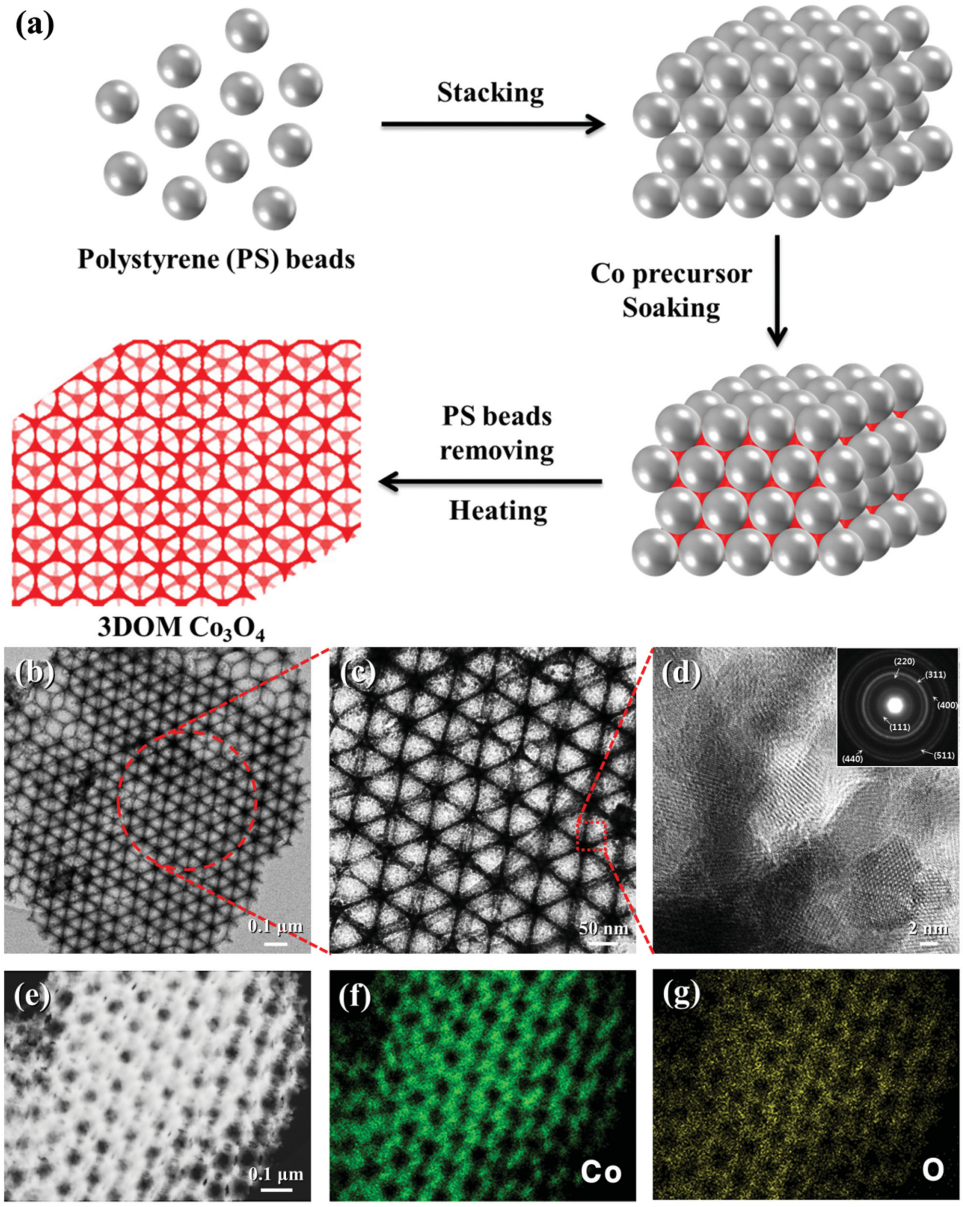


**Figure 1.** a) Schematic image of 3DOM $Co_3O_4$ synthesis, b–d) bright-field HRTEM with SAED pattern (inset), and e–g) dark-field STEM with elemental mapping of cobalt and oxygen of 3D framed cobalt oxide (3DOM $Co_3O_4$).

selected area electron diffraction (SAED) pattern as well as scanning transmission electron microscopy (STEM) elemental mapping of 3DOM $Co_3O_4$. The TEM images reveal highly ordered and uniform hierarchical framework with regular porosity (average pore diameter of ≈150 nm) (Figure 1b,c) created by using PS beads as an effective template. The 3DOM structure is thus a negative of the PS template, where highly concentrated $Co_3O_4$ arranged in a hexagonal pattern is due to the collection of the material in the voids of neighboring beads. Figure 1d shows that 3DOM $Co_3O_4$ is highly crystalline in nature evident by clear fringes observed and the obtained SAED pattern (Figure 1d, inset). Accordingly, the skeletal architecture of 3DOM $Co_3O_4$ is likely to be robust for enhanced electrochemical durability. Furthermore, the composition and distribution of elements of 3DOM $Co_3O_4$ is revealed by STEM elemental mapping (Figure 1e–g) where virtually identical cobalt and oxygen maps are observed in Figure 1f and Figure 1g, respectively. Additionally, the morphology of 3DOM $Co_3O_4$ is also verified by scanning electron microscopy (SEM) where both high and low magnification images reveal highly ordered "honeycomb-like" 3D hierarchically framework consistent with the result of TEM analysis with each cluster having microscale dimensions. (Figure S1, Supporting Information) The microsized pores facilitate diffusion of oxygen in and out of the catalyst structure much more effectively during ORR and OER, respectively. This is attributed to the relatively larger sizes of voids having lowered oxygen diffusion resistances compared to those of nanosized pores. The oxygen readily being transported in and out of the structure could then lead to reduced overpotential for the onsets of ORR and OER, improving the activity of the catalyst.

small NANO MICRO

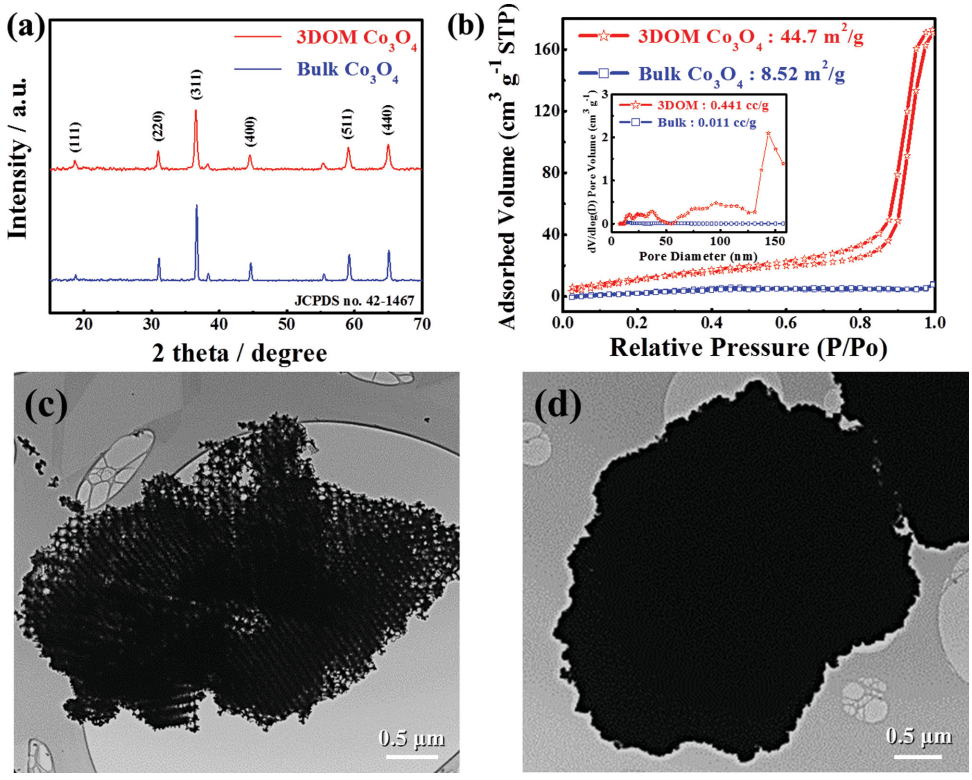


**Figure 2.** a) XRD patterns of 3DOM $Co_3O_4$ (top) and bulk $Co_3O_4$ (bottom). b) Nitrogen adsorption–desorption isotherms and pore size distribution of 3DOM $Co_3O_4$ (top star) and bulk $Co_3O_4$ (bottom square). c,d) TEM images of 3DOM $Co_3O_4$ (left) and bulk $Co_3O_4$ (right). Each scale bar is 0.5 μm.

Next, X-ray diffraction (XRD) has been carried out to confirm the crystal structure of 3DOM $Co_3O_4$ (**Figure 2**a, top) and compared to that of bulk $Co_3O_4$ (bottom) prepared as a control, where the bulk $Co_3O_4$ has been synthesized by a simple hydrothermal reaction followed by annealing at the same temperature applied to the preparation of 3DOM $Co_3O_4$ (See Supporting Information). The XRD patterns of both 3DOM and bulk $Co_3O_4$ are indicative of cubic spinel crystal structure consistent with that of typical spinel cobalt oxide (space group: *Fd3m* (227), JCPDS No. 42-1467).[28,29] The crystal orientations of 3DOM $Co_3O_4$ previously confirmed by the obtained SAED pattern (Figure 1d, inset) matches the peaks of the XRD pattern. Despite having the same crystal structure, the morphology of 3DOM and bulk $Co_3O_4$ is structurally different as shown by TEM images in Figure 2c,d, respectively, where the innovative morphology of 3DOM $Co_3O_4$ is the most crucial requisite determining improved electrochemical performance. Overall, 3DOM $Co_3O_4$ exhibits a highly regular 3D ordered mesoporous structure, whereas bulk $Co_3O_4$ is observed to consist of highly compact crystals of $Co_3O_4$ particles without any signs of pore formation. As observed in SEM and TEM images, hierarchically ordered and interconnected inorganic frames result in a honeycomb like mesoporous 3DOM $Co_3O_4$ structure, where the 3D open structure gives rise to a high surface area exposing more active sites for bifunctional catalysis. This is verified by the $N_2$ adsorption–desorption isotherms (Figure 2b), where 3DOM $Co_3O_4$ (top star) results in a type IV isotherm with a type II contribution having a type H3 hysteresis loop in the higher relative pressure ($P/P_0$) range of 0.6–1.0, which are characteristics of a mesoporous material.[30–33] In terms of the specific surface area, the Brunauer-Emmet-Teller (BET) measurement has resulted in 44.7 $m^2$ $g^{-1}$ for 3DOM $Co_3O_4$, which is about five times greater than that of bulk $Co_3O_4$ (8.52 $m^2$ $g^{-1}$). Similarly, significantly larger pore volume of 3DOM $Co_3O_4$ of 0.441 $cm^3$ $g^{-1}$ has been obtained, which is found to be more than 40 times greater than that of bulk $Co_3O_4$ (0.011 $cm^3$ $g^{-1}$). These results obtained with 3DOM $Co_3O_4$ are attributed to the existence of mesopores consistently observed in the results of pore size distribution (Figure 2b, inset). The high surface area of the well-ordered mesoporous structure of 3DOM $Co_3O_4$ not only facilitates the diffusion of oxygen and electrolyte but also increases catalyst active surface area utilization resulting in improved electrochemical battery performance. The electronic structure of 3DOM $Co_3O_4$ has been revealed by X-ray photoelectron spectroscopy (XPS) where the existence of Co and O has been confirmed as expected. Furthermore, the high-resolution XPS spectrum of Co 2p, showing two pairs of spin–orbit doublets, deconvoluted spectra suggest the coexistence of $Co^{2+}/Co^{3+}$ cations in 3DOM $Co_3O_4$ (Figure S2, Supporting Information).[27] The bifunctional catalytic activity of spinel $Co_3O_4$ toward both ORR and OER is attributed to the mixed valences of coexisting cobalt cations facilitating electron transfer by providing donor–acceptor chemisorption sites for both reversible oxygen adsorption and desorption in the cubic spinel structure. This results in relatively low activation energies for ORR and OER for spinel $Co_3O_4$ leading to accelerated rates of the oxygen surface reactions.

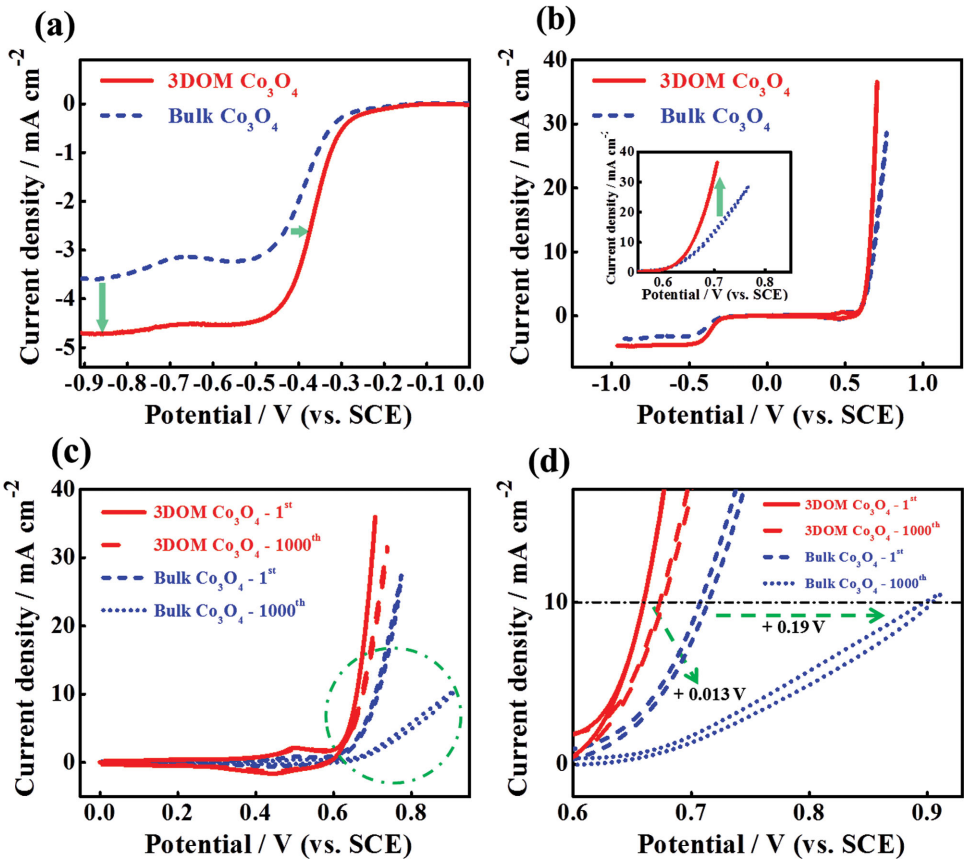


**Figure 3.** Rotating Disk Electrode (RDE) half-cell tests: a) ORR polarization curves and b) full range ORR and OER polarization curves in $O_2$-saturated and $N_2$-saturated 0.1 M KOH solution at room temperature (rotation speed 1600 rpm, sweep rate 10 mV $s^{-1}$) for 3DOM $Co_3O_4$ (solid line) and bulk $Co_3O_4$ (dashed line). Inset is detailed comparison between OER activities of the prepared catalysts (3DOM: solid line, Bulk: dotted line). c,d) OER polarization curves during cycling durability tests in $N_2$-saturated 0.1 M KOH solution at room temperature (rotation speed 1600 rpm, sweep rate 50 mV $s^{-1}$) for 3DOM $Co_3O_4$ (solid and dashed lines) and bulk $Co_3O_4$ (short dashed and dotted lines) before and after 1000 cycles. Test results in the circle are enlarged to verify the detailed change in working potential of prepared catalysts.

To investigate the advanced morphological effect of 3DOM $Co_3O_4$ on bifunctional electrocatalytic activity, three-electrode half-cell testing has been conducted in both the ORR and OER regimes. In terms of ORR (**Figure 3**a), the polarization curve obtained with 3DOM $Co_3O_4$ (solid line) exhibits positively shifted onset and half-wave potentials (–0.197 and –0.360 V vs Saturated Calomel Electrode (SCE)) as well as a much higher magnitude of limiting current density (–4.71 mA $cm^{-2}$). In comparison, the bulk shaped $Co_3O_4$ (dash line) shows limited ORR activity, exhibiting relatively negative shifted onset and half-wave potentials (–0.234 and –0.394 V vs SCE) and lower magnitude of limiting current density (–3.57 mA $cm^{-2}$). A similar trend of morphological effect is observed with the activity of OER (Figure 3b), where 3DOM $Co_3O_4$ (solid line) displays higher OER activity by offering improvement in current density of 21.17 mA $cm^{-2}$ at 0.7 V versus SCE. Relatively lower ORR and OER Tafel slopes of 3DOM $Co_3O_4$ have resulted in 72 and 58 mV per decade, respectively, in comparison to those of bulk $Co_3O_4$ (84 and 90 mV per decade) indicative of faster kinetics during the electrocatalytic reactions of oxygen as expected (Figure S3, Supporting Information). This could be derived from the enlarged catalytic surface area of 3DOM $Co_3O_4$ compared to that of bulk shaped spinel cobalt oxide. The ORR activity enhancement of 3DOM $Co_3O_4$ is attributed to the extended surface area and 3D architectural morphology previously confirmed by BET and TEM characterizations, respectively (Figure 2). Since the electrochemical oxygen reactions such as ORR and OER are based on surface catalytic reactions, the larger exposed area typically provides more active sites towards ORR and OER for the enhancement of electrocatalytic performances. Compared to bulk $Co_3O_4$, 3DOM $Co_3O_4$ has a large number of pores allowing the advanced catalyst to have drastically expanded surface area and thereby increased number of catalytic active sites. In addition to the effect of improved porosity, the 3D hierarchical architecture of 3DOM $Co_3O_4$ also contributes to the enhanced ORR and OER performance by providing consistently interconnected pathways for the transfer of electrons which are rigorously generated or consumed by the highly catalytic oxygen reactions. The number of electron transferred has been obtained by Koutecky–Levich (K–L) plots and 3DOM $Co_3O_4$ shows 3.9 over a wide range of potential transferring close to four electrons (Figure S4, Supporting Information). In addition to the excellent bifunctional electrocatalytic activity of 3DOM $Co_3O_4$ observed, electrochemical durability has been investigated

by conducting cyclic voltammetry (CV) in the high potential OER region, which exposes catalysts under more severe conditions (Figure 3c). After 1000 CV cycles in the OER potential range, the recorded potential of 3DOM $Co_3O_4$ at 10 mA $cm^{-2}$ has increased only by 13 mV (solid to dash), while bulk $Co_3O_4$ has demonstrated a much larger increase of 190 mV (short dash to dot). The electrochemical durability results in terms of OER potential change at 10 mA $cm^{-2}$ are more clearly presented in Figure 3d, where bulk $Co_3O_4$ is observed to degrade more severely after repeated cycling, demonstrated by larger positive potential shift. Interestingly, the final OER current density of 3DOM $Co_3O_4$ after cycling is higher than the initial OER performance of bulk $Co_3O_4$, demonstrating its high electrocatalytic activity and durability toward OER.

Precious metal-based bifunctional catalyst created by mixing Pt/C and Ir/C has also been evaluated by half-cell testing including ORR and OER activity tests and OER cycling durability test to further verify the practical viability of 3DOM $Co_3O_4$ (Figure S6, Supporting Information). The ORR activity of the precious bifunctional catalyst is relatively higher than that of 3DOM $Co_3O_4$. With respect to OER activity, however, 3DOM $Co_3O_4$ shows comparable OER performance to that of the precious bifunctional catalyst. The slightly lower OER activity of 3DOM $Co_3O_4$ is compensated by its significantly lower price and higher abundance than the precious metal-based catalysts, Pt/C and Ir/C. More importantly, however, the precious catalysts are only unifunctionally active toward either ORR or OER, which is why both Pt/C and Ir/C are required to demonstrate ORR and OER, respectively. Utilizing 3DOM $Co_3O_4$ as a bifunctionally active catalyst, on the other hand, allows demonstration of both ORR and OER on a single active catalyst.

In terms of OER cycling durability test, even though the initial cycle of the precious catalyst slightly outperforms 3DOM $Co_3O_4$ with respect to the onset potential and current density, Pt/C + Ir/C becomes very unstable only after 200 cycles demonstrating significantly lowered OER activity. Furthermore, the OER potential is positively shifted by 350 mV to reach 10 mA $cm^{-2}$ only after 200 cycles as opposed to the shift of only 13 mV after 1000 cycles obtained with 3DOM $Co_3O_4$ (Figure S6c, Supporting Information). In addition to excellent oxygen electrocatalytic activities, it is necessary for catalysts to have good electrochemical stability under the severe environment high potentials incurred during OER. The robust hierarchically ordered frames of 3DOM $Co_3O_4$ effectively helps to withstand harsh cycling conditions by demonstrating significantly smaller performance degradation and maintaining the original morphology. The durability of 3DOM $Co_3O_4$ after cycling is verified by performing TEM analysis in terms of morphology, where the initial mesoporous framework with highly ordered architecture is observed to remain intact (Figure S7, Supporting Information). The neighboring particles are Vulcan Carbon physically mixed with 3DOM $Co_3O_4$ during electrode fabrication. This trend directly correlates with the results of the previous ORR and OER tests in that the electrocatalytic durability of 3DOM $Co_3O_4$ is extremely high by exhibiting only 13 mV of potential shift at 10 mA $cm^{-2}$ even after 1000 cycles as well as undergoing no morphological changes during the long term electrochemical test. A relatively small shift of 13 mV of the OER potential at 10 mA $cm^{-2}$ after cycling is likely due to highly robust 3DOM structure, where a considerable amount of internal pores is maintained, resulting in the maintenance of a highly active surface area and catalytic activity even after OER cycling. Bulk $Co_3O_4$, on the other hand, demonstrates a much more severe OER potential shift of 190 mV after cycling, resulting in significant OER activity loss.

To demonstrate electrochemically bifunctional catalytic performance of 3DOM $Co_3O_4$ in realistic environments, electrically rechargeable zinc–air battery prototypes have been fabricated and electrochemical performances have been evaluated. At the air electrode, the as-synthesized catalyst has been incorporated into a nickel-based single-layered air electrode (Supporting information). **Figure 4**a presents a schematic illustration of the rechargeable zinc–air battery design utilized in this study, and Figure 4b presents a working prototype consisting of two zinc–air batteries connected in series operating in ambient conditions utilizing atmospheric air as the source of fuel. Figure 4c presents charge and discharge polarization curves (V vs *i*) of air electrodes with 3DOM $Co_3O_4$, bulk 3DOM $Co_3O_4$, and Pt/C + Ir/C galvanodynamically obtained in a wide range of applied current density. With respect to open circuit voltage (OCV), the precious catalyst demonstrates 1.42 V, which is slightly higher than that of 3DOM $Co_3O_4$ (1.36 V), whereas bulk $Co_3O_4$ results in the lowest OCV (1.28 V). The order of the above values are related to the potential of each catalyst most likely based on the intrinsic resistance, which are in the same order of performance demonstrated by ORR and OER half-cell electrochemical tests. Superior discharge and charge voltages of 3DOM $Co_3O_4$ are clearly observed in the galvanodynamic discharge and charge polarization profiles at the applied current range. During discharge, 3DOM $Co_3O_4$ shows a remarkably low rate of potential drop while current is increasing by maintaining the battery potential above 1.2 V until the current density passes 30 mA $cm^{-2}$. However, bulk $Co_3O_4$ quickly loses its discharge potential, exhibiting 1.2 V at 5 mA $cm^{-2}$, with the potential gap between the discharge profiles of 3DOM $Co_3O_4$ and bulk $Co_3O_4$ gradually increased at higher current densities. The potential difference between 3DOM $Co_3O_4$ and Pt/C + Ir/C is relatively large at a low current due to the high OCV of the precious catalyst. At high discharge current, however, the difference is very small, elucidating that 3DOM $Co_3O_4$ has a comparable rate of battery potential drop to that of Pt/C + Ir/C. During charge, the overall increase of charge potential of 3DOM $Co_3O_4$ is slightly higher than that of Pt/C + Ir/C, but far lower than that of bulk $Co_3O_4$. From the potential gap between discharge and charge polarization curves measured at high current density (50 mA $cm^{-2}$), the overpotential of the catalysts can be obtained. Pt/C + Ir/C presents 0.76 V, 3DOM $Co_3O_4$ shows 0.85 V, and lastly $Co_3O_4$ displays 1.07 V, indicating the comparable catalytic activity of 3DOM $Co_3O_4$ to that of Pt/C + Ir/C. The results correspond to the trend of overpotentials between ORR

  

www.MaterialsViews.com

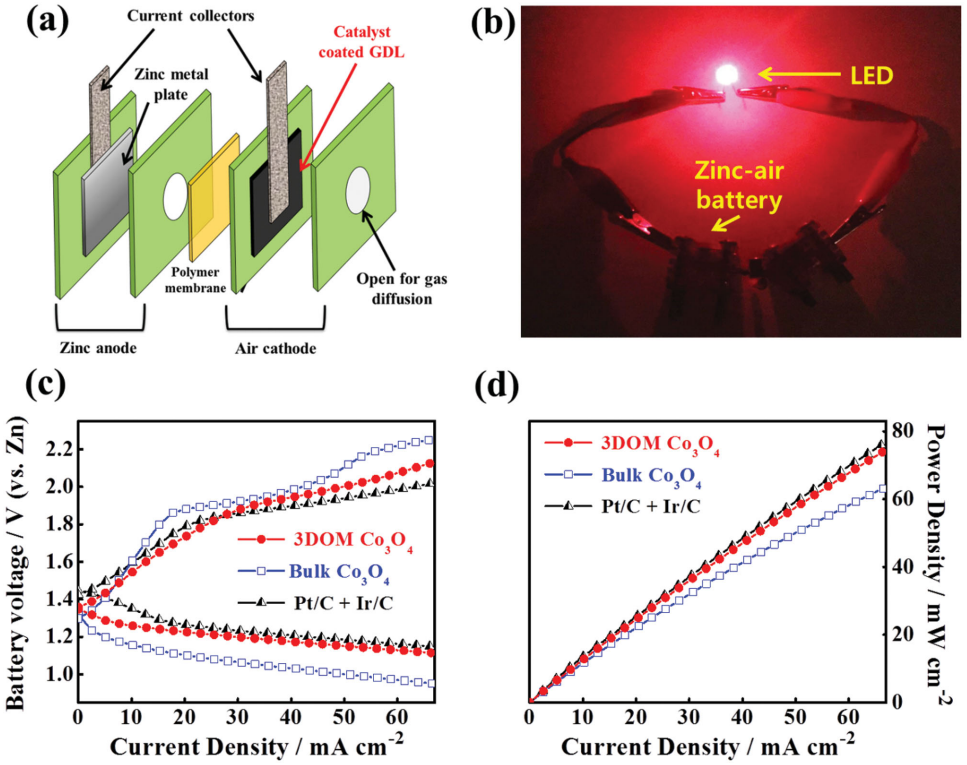


**Figure 4.** Electrochemical performance of the electrically rechargeable zinc–air battery prototypes using 3DOM $Co_3O_4$, bulk $Co_3O_4$, and Pt/C + Ir/C as air electrode bifunctional catalysts. a) Schematic illustration of rechargeable zinc–air battery design. b) Prototype in operation consists of two zinc–air batteries in ambient conditions. c,d) Galvanodynamic charge and discharge polarization curves and corresponding power density plots of air electrode bifunctional catalysts such as 3DOM $Co_3O_4$ (filled circles), bulk $Co_3O_4$ (open squares), and Pt/C + Ir/C (black triangles).

and OER evaluated by electrochemical half-cell tests. Power density curves are also acquired by applying current density and measuring discharge voltage within the applied range of current density (Figure 4d). 3DOM $Co_3O_4$ presents highly similar power density to that of Pt/C + Ir/C, whereas bulk $Co_3O_4$ shows much lower values. The excellent rechargeable zinc–air battery performances of 3DOM $Co_3O_4$ combined with its great cost competitiveness over the precious metal-based bifunctional catalyst clearly demonstrate its potential for practical usage in commercially rechargeable zinc–air batteries.

In **Figure 5**, galvanostatic charge and discharge battery cycling tests have been performed by applying 10 mA $cm^{-2}$ and 2 h cycle periods so as to investigate the rechargeability of the catalyst coated air electrodes in the zinc–air battery. 3DOM $Co_3O_4$ displays a significantly long battery lifetime over 200 cycles (more than 400 h) without increasing overpotential measured by voltage gap between discharge and charge potentials (Figure 5a). In contrast, bulk $Co_3O_4$ and Pt/C + Ir/C demonstrate limited battery lifetimes by performing only 90 and 7 cycles, respectively, before displaying severely enlarged overpotentials derived from the increased charge potential and decreased discharge potential during cycling (Figure 5b,c). In Figure 5d, the charge and discharge potentials of the catalysts are demonstrated to highlight initial performance and durability of 3DOM $Co_3O_4$ relative to the other tested catalysts. During the first four cycles, Pt/C + Ir/C shows the smallest potential difference of 0.71 V between charge and discharge, and 3DOM $Co_3O_4$ demonstrates comparable potential difference of 0.76 V, whereas bulk $Co_3O_4$ shows the largest difference of 0.84 V (Table S2, Supporting Information). After four cycles, however, Pt/C + Ir/C rapidly loses its catalytic activity toward ORR and OER, resulting in both severely degraded charge and discharge voltages. Furthermore, the performance of Pt/C + Ir/C noticeably declines after six cycles resulting in drastically enlarged charge and discharge potential difference of ≈1.4 V. This severe performance loss is likely due to carbon corrosion at high voltages, as well as dissolution and agglomeration of the precious metal catalyst.[34] Although bulk $Co_3O_4$ exhibits longer cycle life than the precious metal catalysts, its rechargeable battery performance also rapidly decreases after 90 cycle, which is inferior compared to stable charge and discharge voltages of 3DOM $Co_3O_4$ over 200 cycles.

Conclusively, all of electrochemical characterizations such as half-cell testing, galvanodynamic and galvanostatic charge and discharge cycling tests have demonstrated consistent trends in performances including electrocatalytic activity and durability of the catalysts. In comparison to other electrocatalysts, 3DOM $Co_3O_4$ introduces highly advanced and innovative morphology and a 3D hierarchical honeycomb-like mesoporous structure, which leads to improved electrochemical durability as well as highly active bifunctional performances (discharge and charge potential: 1.24 and 2.0 V at 10 mA $cm^{-2}$) confirmed by both half-cell testing (1000 OER

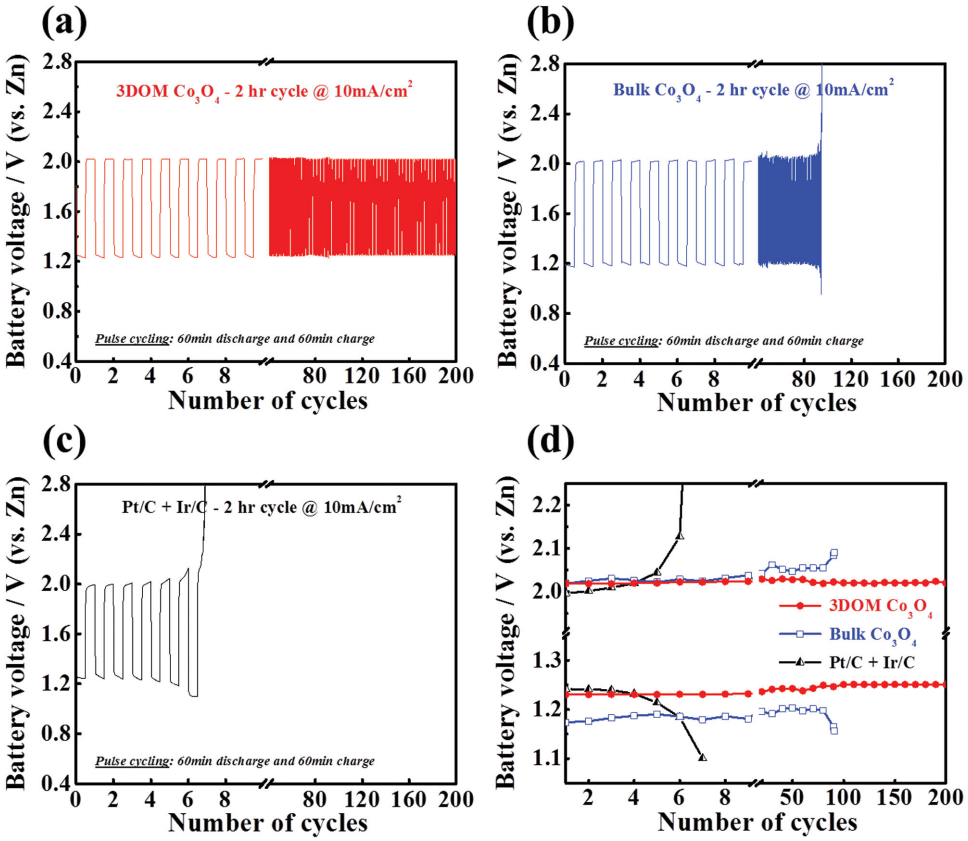


**Figure 5.** Electrochemical galvanostatic charge and discharge cycling curves of the electrically rechargeable zinc–air battery prototypes: a) 3DOM $Co_3O_4$, b) bulk $Co_3O_4$, and c) Pt/C + Ir/C as air electrode bifunctional catalysts. d) The first ten battery cycles for all prepared catalysts for comparing initial performances. Battery operations on ambient conditions (each cycle period 2 h; 1 h for discharge and 1 h for charge, current density 10 mA $cm^{-2}$, pure oxygen gas purged to air electrode).

CV cycles) and rechargeable zinc–air battery cycling experiments (200 charge/discharge cycles).

## Supporting Information

*Supporting Information is available from the Wiley Online Library or from the author.*

## Acknowledgements

*This research was supported by the Natural Sciences and Engineering Research Council of Canada (NSERC) through grants to Z.C. and the University of Waterloo.*

[1] R. Cao, J.-S. Lee, M. Liu, J. Cho, *Adv. Energy Mater.* **2012**, *2*, 816.
[2] J.-S. Lee, S. T. Kim, R. Cao, N.-S. Choi, M. Liu, K. T. Lee, J. Cho, *Adv. Energy Mater.* **2011**, *1*, 34.
[3] F. Cheng, J. Chen, *Chem. Soc. Rev.* **2012**, *41*, 2172.
[4] Y. Li, M. Gong, Y. Liang, J. Feng, J. E. Kim, H. Wang, G. Hong, B. Zhang, H. Dai, *Nat. Commun.* **2013**, *4*, 1805.
[5] D. U. Lee, B. J. Kim, Z. Chen, *J. Mater. Chem. A* **2013**, *1*, 4754.
[6] D. H. W. Park, D. U. Lee, M. G. Park, R. Ahmed, D. M. H. Seo, P. L. F. Nazar2, P. Z. Chen, *ChemSusChem* **2015**, *8*, 8.
[7] D. U. Lee, H. W. Park, M. G. Park, V. Ismayilov, Z. Chen, *ACS Appl. Mater. Interfaces* **2014**, *7*, 902.
[8] J. Masa, W. Xia, I. Sinev, A. Zhao, Z. Sun, S. Grutzke, P. Weide, M. Muhler, W. Schuhmann, *Angew. Chem.* **2014**, *53*, 8508.
[9] X. Liu, M. Park, M. G. Kim, S. Gupta, G. Wu, J. Cho, *Angew. Chem. Int. Ed.* **2015**, *54*, 9654.
[10] X. Liu, W. Liu, M. Ko, M. Park, M. G. Kim, P. Oh, S. Chae, S. Park, A. Casimir, G. Wu, *Adv. Funct. Mater.* **2015**, *25*, 5799.
[11] Z. Chen, A. Yu, D. Higgins, H. Li, H. Wang, Z. Chen, *Nano Lett.* **2012**, *12*, 1946.
[12] G. Nam, J. Park, M. Choi, P. Oh, S. Park, M. G. Kim, N. Park, J. Cho, J.-S. Lee, *ACS Nano* **2015**, *9*, 6493.
[13] T. Y. Ma, S. Dai, M. Jaroniec, S. Z. Qiao, *J. Am. Chem. Soc.* **2014**, *136*, 13925.
[14] H. Cheng, Y.-Z. Su, P.-Y. Kuang, G.-F. Chen, Z.-Q. Liu, *J. Mater. Chem. A* **2015**, *3*, 19314.
[15] J. Suntivich, H. A. Gasteiger, N. Yabuuchi, H. Nakanishi, J. B. Goodenough, Y. Shao-Horn, *Nat. Chem.* **2011**, *3*, 5.
[16] C.-F. Chen, G. King, R. M. Dickerson, P. A. Papin, S. Gupta, W. R. Kellogg, G. Wu, *Nano Energy* **2015**, *13*, 10.
[17] J. I. Jung, H. Y. Jeong, J. S. Lee, M. G. Kim, J. Cho, *Angew. Chem.* **2014**, *53*, 4582.
[18] J. W. D. Ng, M. Tang, T. F. Jaramillo, *Energy Environ. Sci.* **2014**, *7*, 2017.
[19] C. Jin, F. Lu, X. Cao, Z. Yang, R. Yang, *J. Mater. Chem. A* **2013**, *1*, 12170.

[20] M. Prabu, K. Ketpang, S. Shanmugam, *Nanoscale* **2014**, *6*, 3173.
[21] F. Cheng, J. Shen, B. Peng, Y. Pan, Z. Tao, J. Chen, *Nat. Chem.* **2011**, *3*, 79.
[22] L. Li, S. Liu, A. Manthiram, *Nano Energy* **2015**, *12*, 852.
[23] Z. Zhuang, W. Sheng, Y. Yan, *Adv. Mater.* **2014**, *26*, 3950.
[24] D. U. Lee, M. G. Park, H. W. Park, M. H. Seo, X. Wang, Z. Chen, *ChemSusChem* **2015**, *8*, 3129.
[25] Y. Liu, D. C. Higgins, J. Wu, M. Fowler, Z. Chen, *Electrochem. Commun.* **2013**, *34*, 125.
[26] D. U. Lee, J. Scott, H. W. Park, S. Abureden, J.-Y. Choi, Z. Chen, *Electrochem. Commun.* **2014**, *43*, 109.
[27] D. U. Lee, J.-Y. Choi, K. Feng, H. W. Park, Z. Chen, *Adv. Energy Mater.* **2014**, *4*, 1301389.
[28] X. Liu, G. Qiu, X. Li, *Nanotechnology* **2005**, *16*, 3035.
[29] X. Lu, H. Chan, C.-L. Sun, C.-M. Tseng, C. Zhao, *J. Mater. Chem. A* **2015**, *3*, 13371.
[30] J.-J. Xu, Z.-L. Wang, D. Xu, F.-Z. Meng, X.-B. Zhang, *Energy Environ. Sci.* **2014**, *7*, 2213.
[31] C. Zhu, D. Wen, S. Leubner, M. Oschatz, W. Liu, M. Holzschuh, F. Simon, S. Kaskel, A. Eychmüller, *Chem. Commun.* **2015**, *51*, 7851.
[32] K. S. Sing, *Pure Appl. Chem.* **1985**, *57*, 603.
[33] C. Weidenthaler, *Nanoscale* **2011**, *3*, 792.
[34] J. Zhang, K. Sasaki, E. Sutter, R. Adzic, *Science* **2007**, *315*, 220.

Received: January 6, 2016
Revised: March 4, 2016
Published online: April 4, 2016